Supplementary information

Resolving the True Origin of Mossy Morphology in Aqueous Zn Batteries

Jianwen Yu[a], Zhongxi Zhao[a], Zhuojun Zhang[a], Jiangfeng Huang[a], Peng Tan[a,b,*]

[a]*Department of Thermal Science and Energy Engineering, University of Science and Technology of China (USTC), Hefei 230026, Anhui, China.*

[b]*State Key Laboratory of Fire Science, University of Science and Technology of China (USTC), Hefei 230026, Anhui, China.*

Email: pengtan@ustc.edu.cn

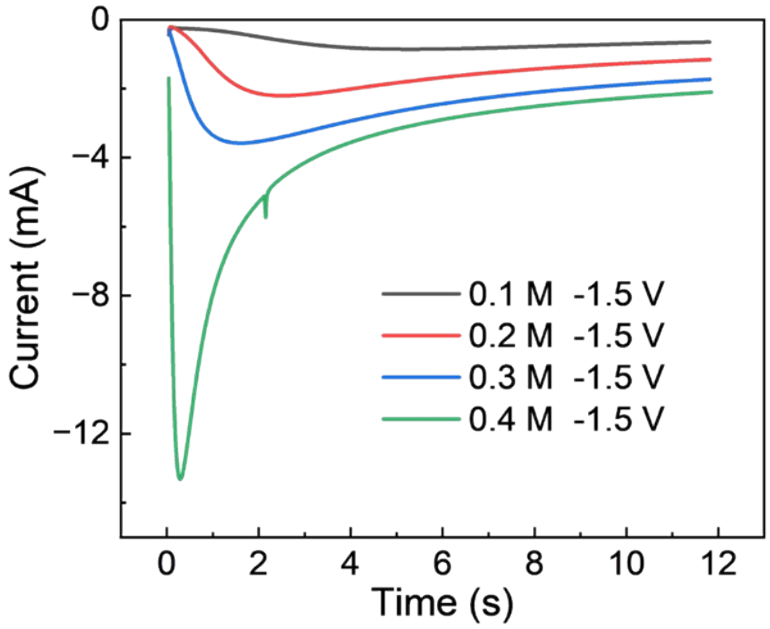

Figure S1. Chronoamperometric curves at different concentrations.

Under constant voltage conditions, the electrochemical reaction area increases due to nucleation, causing the absolute current to rise initially. Once the nucleation covers the entire electrode surface, the electrochemical reaction area decreases, and the current starts to decrease and stabilize.[1] It can be observed that, compared to low concentration, the time to reach the peak current is shorter at high concentrations. At 0.1 M, the time is approximately 4 s, while at 0.4 M, it is less than 0.5 s, indicating that nucleation occurs more rapidly at higher concentrations.

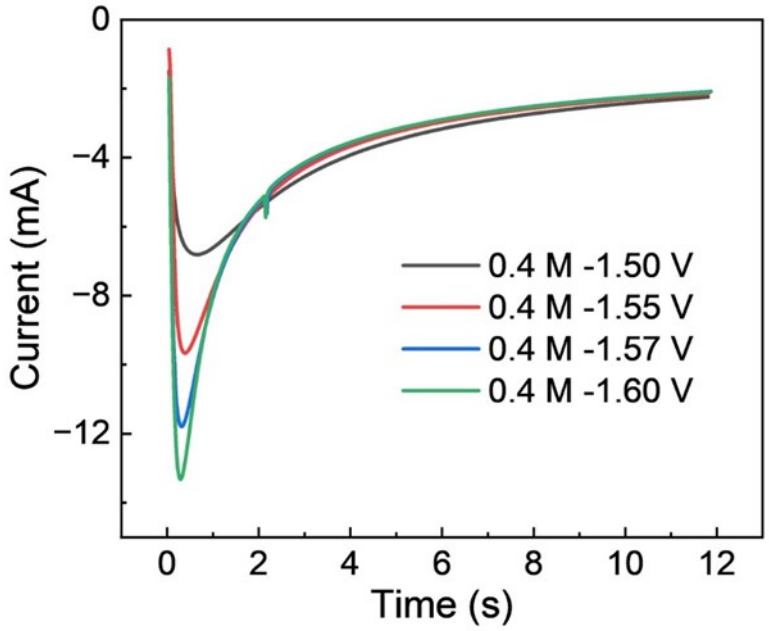

Figure S2. Chronoamperometric curves at different polarization levels.

Similar to concentration, the time to reach the peak current is shorter at high overpotentials compared to low overpotentials. At -1.5 V, the time to reach the peak current is approximately 0.6 s, while at -1.6 V, it is less than 0.3 s, indicating that nucleation occurs more rapidly at higher overpotentials.

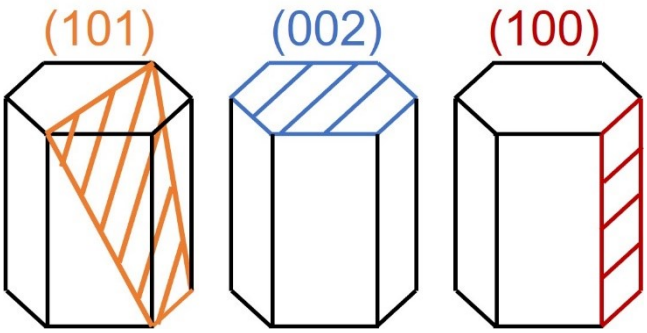

Figure S3. Schematic diagram of three zinc crystal planes.

The (002) facet of zinc, due to its low surface energy, is one of the most stable crystallographic planes and has a hexagonal shape. Under typical conditions, zinc deposition tends to grow along a specific crystallographic orientation, especially at low overpotentials, where the zinc crystals preferentially grow along the most stable planes, such as the (002) facet.[2,3] In Fig. 4b, the deposited material is seen to be composed of hexagonal stacking, indicating the dominance of the (002) facet in the early stages of zinc deposition.

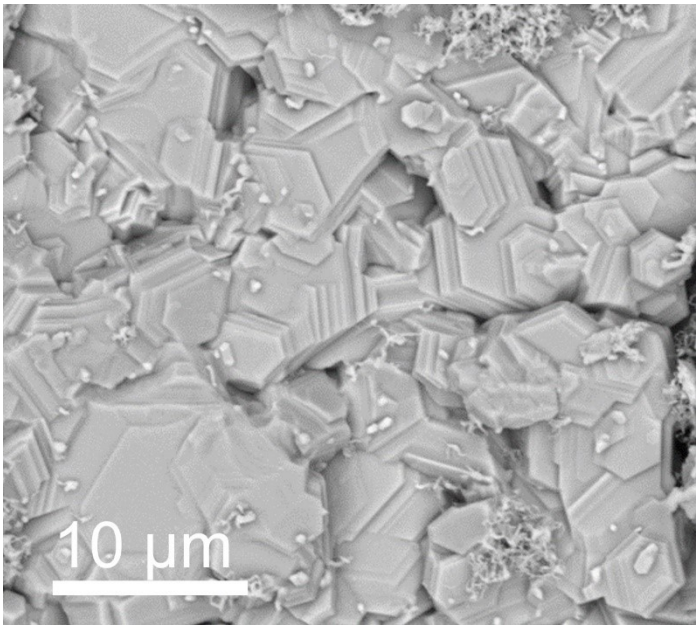

Figure S4. Protrusions formed on the basal plane.

At a certain stage of deposition, protrusions begin to appear on the stacked hexagonal basal planes, and in some areas, these protrusions have even developed into mossy deposits, indicating that the protrusions represent a transition towards mossy deposition.

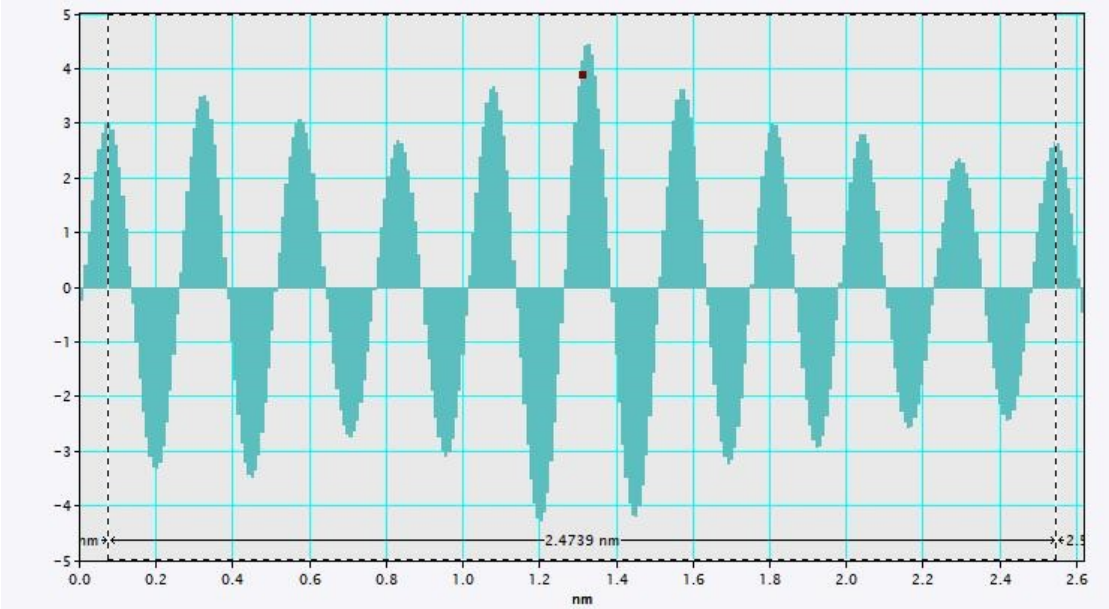

Figure S5. Lattice spacing on the left side of the grain boundary.

After performing a Fast Fourier Transform (FFT) on the region selected to the left of the grain boundary, the two brightest points are chosen. A mask is applied, followed by an inverse Fourier transform. The resulting alternating light and dark stripes are measured for the distance between 10 of them. The measured distance is 2.47 Å, which is calibrated as the (002) plane of zinc.[4]

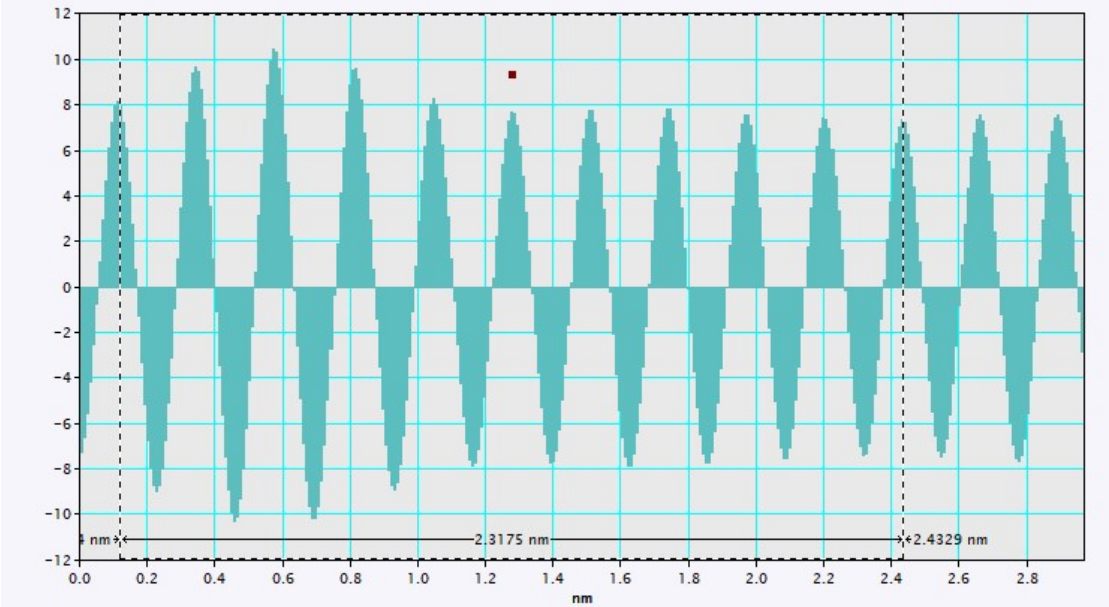

Figure S6. Lattice spacing on the right side of the grain boundary.

A similar analysis is performed on the region to the right of the grain boundary, where the lattice spacing is found to be 2.3 Å, calibrated as the (100) plane of zinc.[5] This indicates that during the growth process of the whiskers, the crystal orientation changes, leading to the bending of the whiskers.

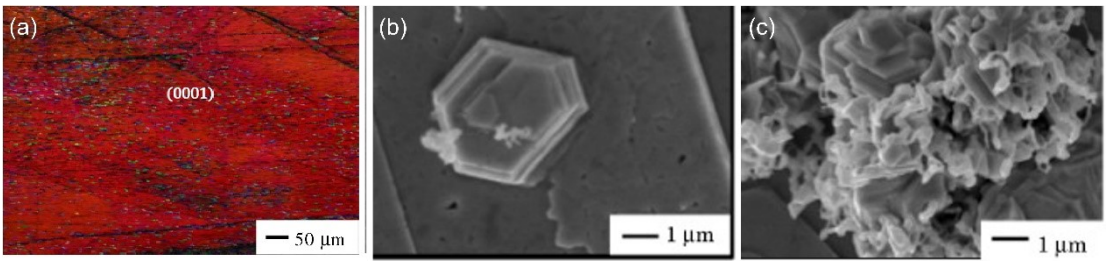

Figure S7. Electrodeposition on (0001) single-crystal zinc.[6] (a) The EBSD analysis of the (0001) single-crystal zinc. (b) Epitaxial growth on the (0001) plane. (c) Formation of mossy morphology on the (002) plane.

Mitsuhashi et al. prepared single-crystal zinc with (0001) orientation, which corresponds to the (002) plane in three-index notation.[6] They conducted electrodeposition experiments on this substrate and found that the initial deposition exhibited epitaxial growth of hexagonal terraces on the (002) plane. When the capacity was further increased, moss-like deposits formed on the surface of these terraces, as shown in Figure S7c. In contrast, when the same experiment was performed on polycrystalline zinc, moss-like deposits did not appear at this capacity level, indicating that reducing the presence of the (002) plane effectively suppressed the formation of mossy deposits. Therefore, we conclude that the (002) plane is the most probable initial condition leading to the formation of mossy zinc and specifically calculated the diffusion energy barriers on the (002) basal plane and for interlayer diffusion.

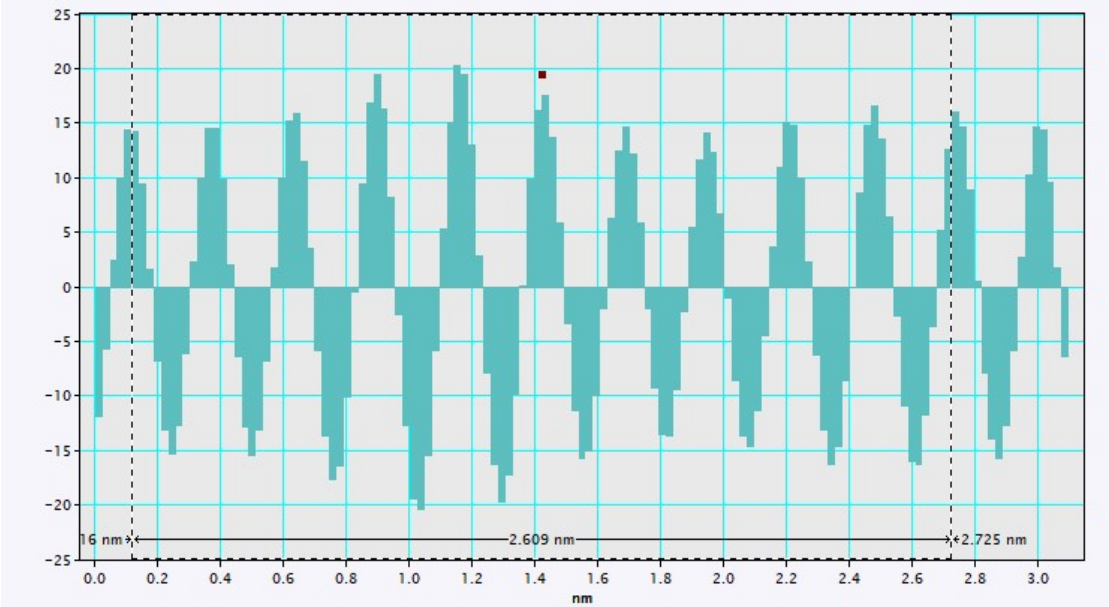

Figure S8. Lattice spacing within the boundary.

Lattice spacing analysis is performed on the interior of the edges of the deposited hexagonal zinc, with a measured value of 2.6 Å.

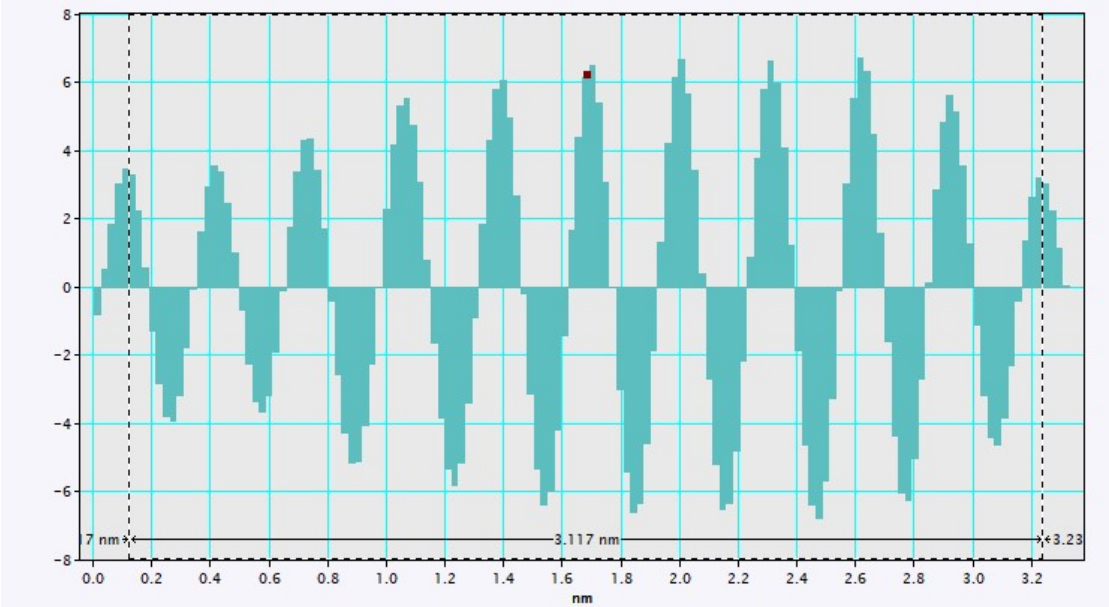

Figure S9. Lattice spacing outside the boundary

Lattice spacing analysis is performed on the exterior of the light-dark boundary of the deposited hexagonal zinc, yielding a value of 3.1 Å. Combined with the element mapping indicating the presence of oxygen and the significant difference in lattice spacing compared to the interior of the boundary, it is concluded that the exterior of the hexagonal zinc deposit is coated with a layer of zinc oxide.

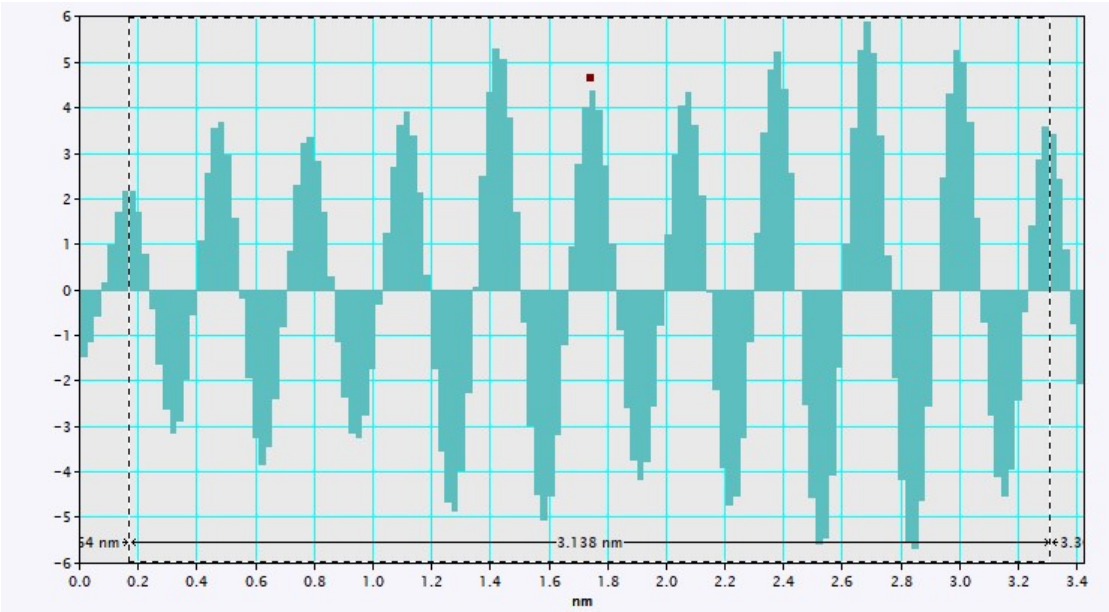

Figure S10. Lattice spacing analysis at 11.7 nm from the edge under low polarization. At low overpotentials, the deposited hexagonal zinc shows no obvious light-dark boundary. Lattice spacing analysis conducted on a region 11.7 nm from the edge yields a value of 3.1 Å, which is the same as the lattice spacing measured on the exterior of the boundary at high overpotentials. This is identified as zinc oxide, indicating that low overpotentials cause the oxide layer to thicken.

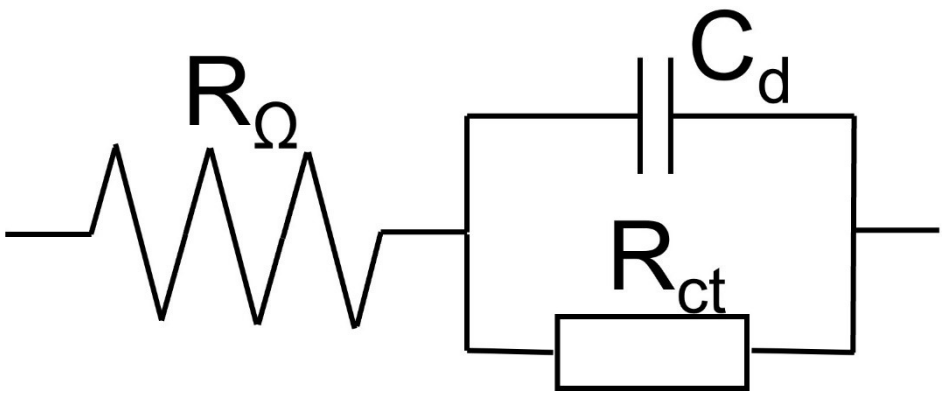

Figure S11. The corresponding equivalent circuit model used for fitting.

R_Ω, C_d, and R_{ct} represent ohmic resistance, double-layer capacitance, and charge transfer resistance, respectively. Since the EIS curve does not show a clear linear segment, the Warburg impedance representing mass transport is not included in the model.

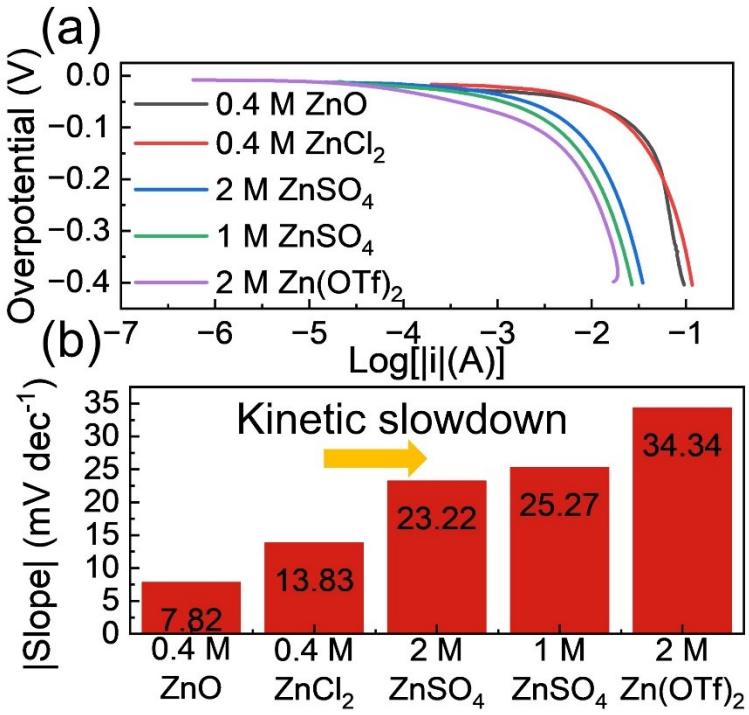

Figure S12. Tafel tests in different types of electrolytes. (a) Tafel curves in different types of electrolytes. (b) Tafel slope analysis.

The physical significance of the Tafel slope can be understood as the change in overpotential required for a tenfold change in current density. A smaller Tafel slope indicates that less driving force is needed to increase the current density by a certain amount, suggesting better reaction kinetics.[7] Therefore, based on the slope, the kinetics in 0.4 M ZnO, 0.4 M $ZnCl_2$, 2 M $ZnSO_4$, 1 M $ZnSO_4$ and 2 M $Zn(OTf)_2$ can be ranked from best to worst.

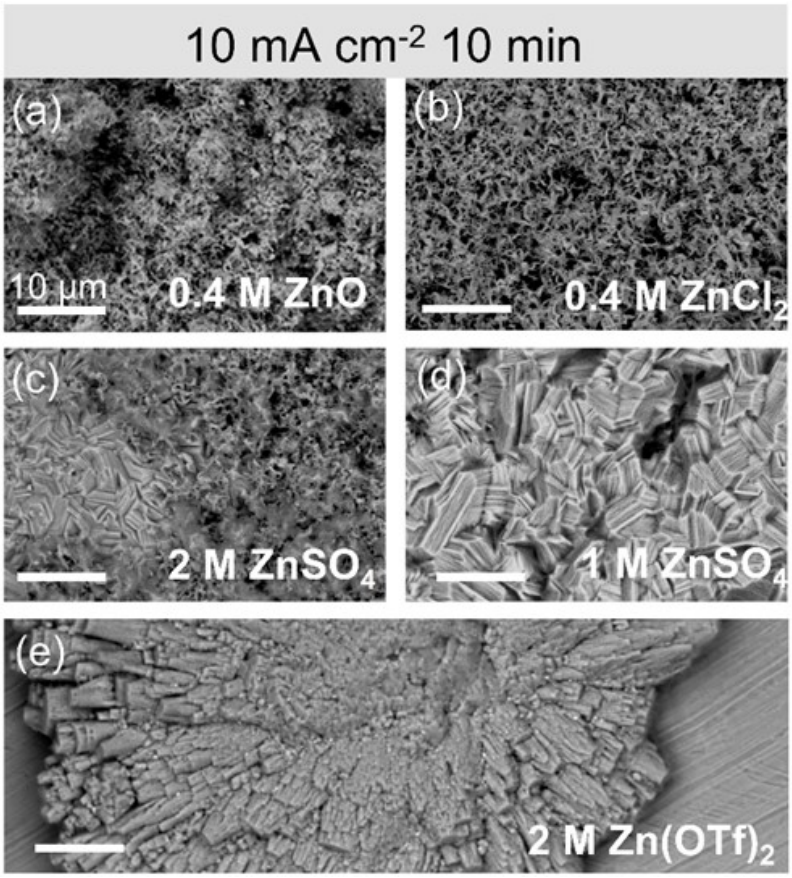

Figure S13. Deposition morphologies in different types of electrolytes under 10 mA cm^{-2} for 10 min. (a) In 0.4 M ZnO. (b) In 0.4 M $ZnCl_2$. (c) In 2 M $ZnSO_4$. (d) In 1 M $ZnSO_4$. (e) In 2 M $Zn(OTf)_2$.

After 10 min of deposition at 10 mA cm^{-2}, the deposition morphologies observed in the four electrolytes were mossy, mossy, partially mossy, stacked plate-like, and radiated block-like morphologies, respectively. This corresponds to the previous Tafel slopes, indicating that the formation of mossy morphology is related to fast reaction kinetics.

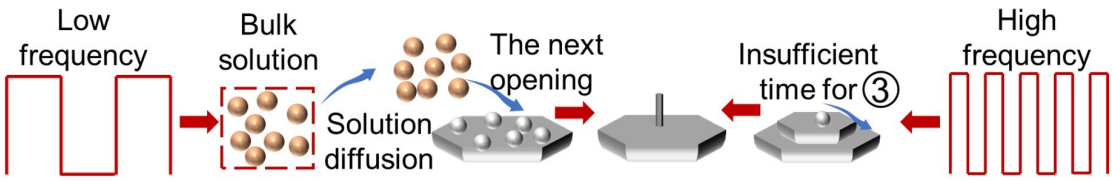

Figure S14. The influence of pulse frequency

At low frequencies, the prolonged relaxation allows more zincate ions to diffuse from the bulk solution to the electrode surface, which are then rapidly reduced during the next pulse, resulting in Zn atoms accumulation and one-dimensional vertical growth. At high frequencies, the short relaxation time is insufficient to support interlayer diffusion, which also leads to mossy deposition.

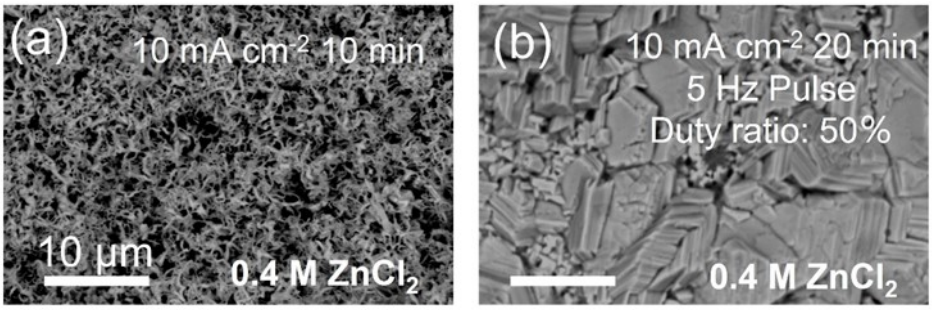

Figure S15. Pulse charging tests in 0.4 M $ZnCl_2$ solution. Deposition morphology images under (a) no pulse and (b) pulse.

The non-pulsed group was deposited at 10 mA cm^{-2} for 10 min, while the pulsed group was deposited for 20 min with a pulse frequency of 5 Hz and a 50% duty cycle. The non-pulsed group exhibits a mossy morphology, whereas the pulsed group shows a gravel-like morphology. This indicates that the suppression strategy is effective beyond alkaline electrolytes, demonstrating a degree of universality.

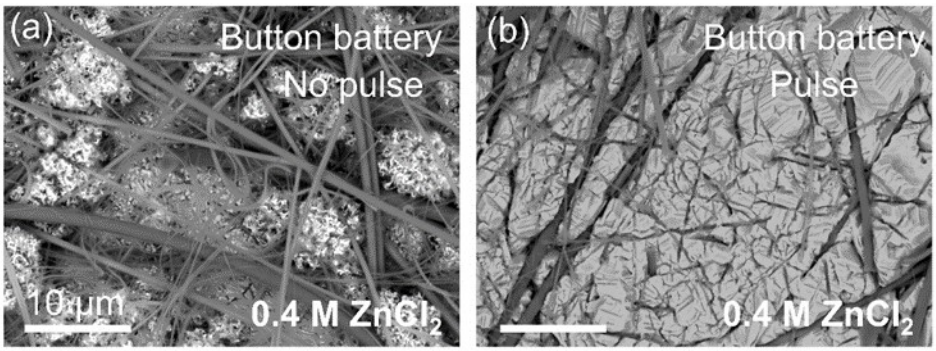

Figure S16. Pulse charging tests in button batteries. Deposition morphology images under (a) no pulse and (b) pulse.

Regarding the applicability of this mechanism in other battery configurations, we also conducted experiments in commonly used button batteries. As shown in Figure S16, using 0.4 M $ZnCl_2$ as the electrolyte and the same charging conditions as in Figure S15, the zinc deposition morphologies under pulsed and non-pulsed conditions in a button battery configuration were compared. Although the separator influences the morphology to some extent, it is evident that the non-pulsed condition still results in mossy deposits, while the pulsed condition leads to a gravel-like structure. This confirms the universality of the mechanism across different battery configurations.

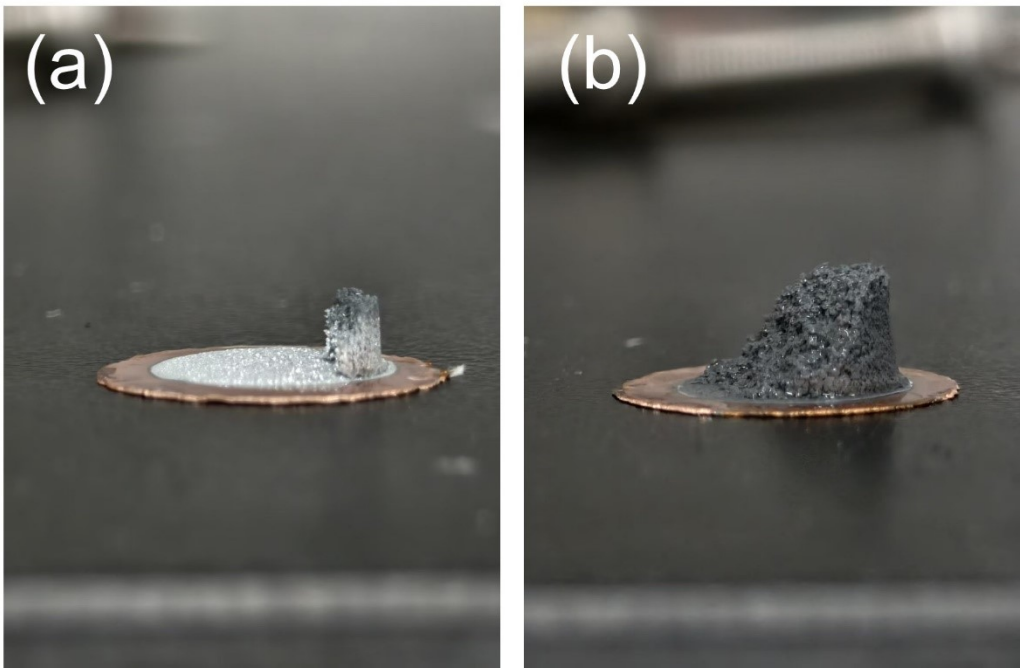

Figure S17. Morphologies of negative electrode deposits after short-circuit tests with and without K_2SnO_3 additive. (a) With K_2SnO_3 additive. (b) Without K_2SnO_3 additive. After deposition with the addition of K_2SnO_3, the volume of the deposit is significantly reduced compared to the no-additive group. Only at the bottom of the electrode, where the concentration is higher, more deposition occurs, and most of the deposit is silvery white, indicating a dense structure. In contrast, the no-additive group exhibits black, loose deposition, which has already bridged the positive and negative electrodes in the middle of the electrode, suggesting that the addition of K_2SnO_3 effectively suppresses the uneven deposition.

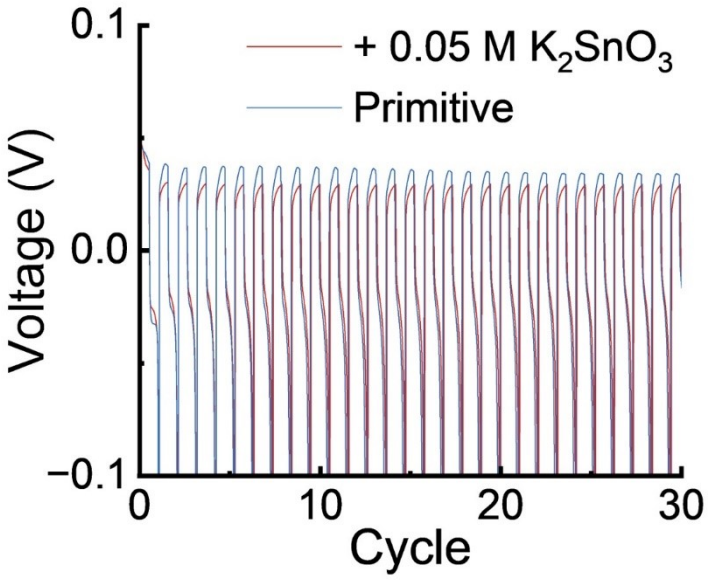

Figure S18. Voltage curves during the initial 30 cycles.

The overpotential of the Sn additive group was initially smaller than that of the pristine group.

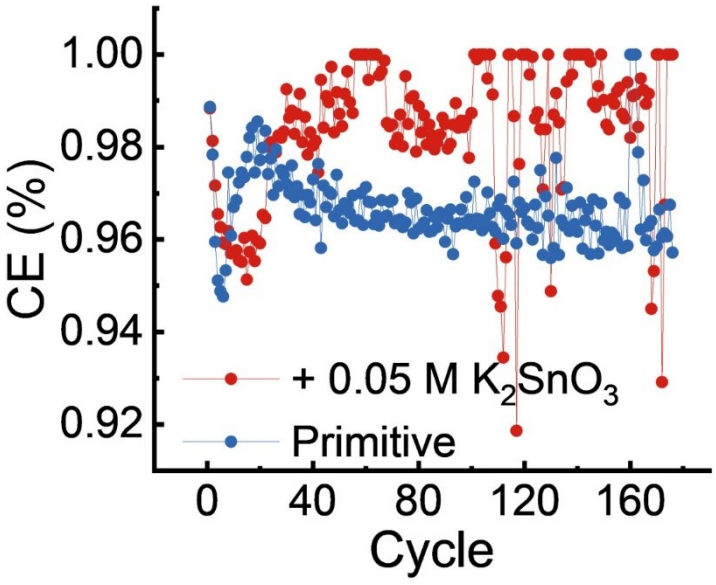

Figure S19. Coulombic efficiencies of two groups.

For most of the cycles, the Coulombic efficiency of the additive group was higher than that of the pristine group. The average Coulombic efficiencies over 176 cycles were 98.35% and 96.68% for the two groups, respectively, indicating that the morphology improved by the Sn additive contributes to performance enhancement.

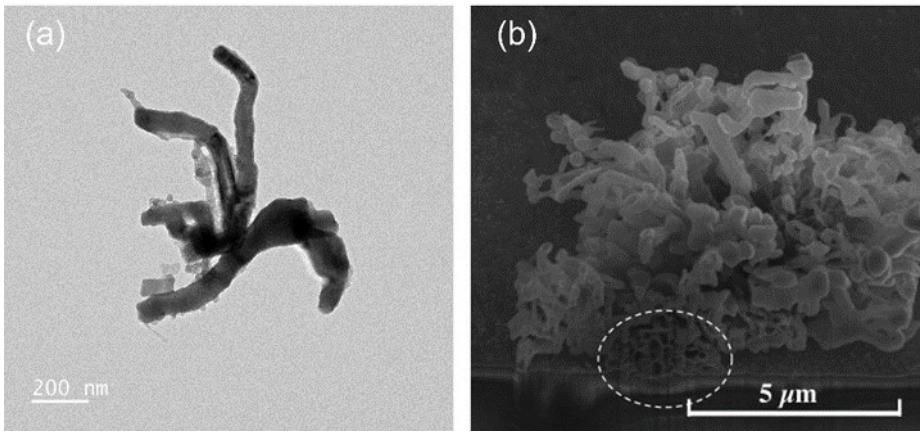

Figure S20. Comparison between mossy zinc and mossy lithium. (a) Mossy zinc. (b) Mossy lithium.[8]

Mossy lithium deposition represents a common morphology in lithium metal batteries, compared with mossy zinc, they may differ in size, which could be attributed to the inherent properties of the metals, such as differences in hardness and strength. However, in terms of morphology, both consist of twisted, ribbon-like structures, as shown in Figure S20. Unlike lithium dendrites that prefer high polarization conditions, mossy lithium tends to form under low polarization conditions[8–12]. This phenomenon shows remarkable similarity to zinc deposition behavior, making it an excellent direction for future investigation.

SI References

[1] S. Wang, Z. Wang, Y. Yin, T. Li, N. Chang, F. Fan, H. Zhang, X. Li, *Energy Environ. Sci.* **2021**, *14*, 4077.

[2] T. Shen, T. Wei, S. Zhang, H. Liu, C. Li, Z. Li, M. Yang, C. Liu, Y. Pei, *Small Structures* **2025**, *6*, 2400325.

[3] Y. Wang, Z. Deng, B. Luo, G. Duan, S. Zheng, L. Sun, Z. Ye, J. Lu, J. Huang, Y. Lu, *Adv. Funct. Mater.* **2022**, *32*, 2209028.

[4] R. Li, M. Li, Y. Chao, J. Guo, G. Xu, B. Li, Z. Liu, C. Yang, YanYu, *Energy Storage Materials* **2022**, *46*, 605.

[5] Z. Yi, Microstructure Studies of Zinc Electrodeposits in Zinc Metal Batteries, Ph.D., The Hong Kong University of Science and Technology, **2024**.

[6] T. Mitsuhashi, Y. Ito, Y. Takeuchi, S. Harada, T. Ujihara, *Thin Solid Films* **2015**, *590*, 207.

[7] W. Yu, W. Shang, Z. Zhao, Y. Ma, P. Tan, *Electrochimica Acta* **2022**, *425*, 140702.

[8] J. Steiger, D. Kramer, R. Mönig, *Electrochim. Acta* **2014**, *136*, 529.

[9] Y. Zhang, F. M. Heim, N. Song, J. L. Bartlett, X. Li, *ACS Energy Lett.* **2017**, *2*, 2696.

[10] Y. Wang, D. Dang, X. Xiao, Y.-T. Cheng, *Energy Storage Materials* **2020**, *26*, 276.

[11] F. Shen, F. Zhang, Y. Zheng, Z. Fan, Z. Li, Z. Sun, Y. Xuan, B. Zhao, Z. Lin, X. Gui, X. Han, Y. Cheng, C. Niu, *Energy Storage Materials* **2018**, *13*, 323.

[12] F. Orsini, A. Du Pasquier, B. Beaudouin, J. M. Tarascon, M. Trentin, N. Langenhuizen, E. De Beer, P. Notten, *J. of Power Sources* **1999**, *81–82*, 918.